Localized Structures in Indented Shells: A Numerical Investigation

Alice Nasto
Department of Mechanical Engineering,
Massachusetts Institute of Technology,
Cambridge, MA 02139
e-mail: anasto@mit.edu

Pedro M. Reis
Department of Mechanical Engineering
and Department of Civil and
Environmental Engineering,
Massachusetts Institute of Technology,
Cambridge, MA 02139
e-mail: preis@mit.edu

We present results from a numerical investigation of the localization of deformation in thin elastomeric spherical shells loaded by differently shaped indenters. Beyond a critical indentation, the deformation of the shell ceases to be axisymmetric and sharp structures of localized curvature form, referred to as "s-cones," for "shell-cones." We perform a series of numerical experiments to systematically explore the parameter space. We find that the localization process is independent of the radius of the shell. The ratio of the radius of the shell to its thickness, however, is an important parameter in the localization process. Throughout, we find that the maximum principal strains remain below 6%, even at the s-cones. As a result, using either a linear elastic (LE) or hyperelastic constitutive description yields nearly indistinguishable results. Friction between the indenter and the shell is also shown to play an important role in localization. Tuning this frictional contact can suppress localization and increase the load-bearing capacity of the shell under indentation. [DOI: 10.1115/1.4028804]

1 Introduction

Localization of deformation in thin shells arises in scenarios over a large range of length scales. At the macroscopic scale, this problem is relevant to the outer-body shells of automobiles and aircraft, which are often made from double-curved thin metal sheets. Localization in these structures can occur during collisions to cause elastic–plastic denting or crumpling [1–3]. The design of thin-walled structures is bounded by a need for them to be lightweight and slender, but also resistant to deformation by suppressing localization, which can cause permanent damage. This calls for a better understanding of the interplay between geometry and friction of the indenter–shell contact in determining the mechanical response. At the microscopic scale, colloidal capsules [4,5] can buckle elastically into polygonal configurations, under varying osmotic pressure. Indentation, another mode of mechanical loading, is encountered in the mechanical testing through atomic force microscopy (AFM) of bacteria [6], virus capsids [7,8], and microcapsules [9]. In AFM, a probe with a sharp tip scans an object with nanometric resolution [10], such that the curvature of the tip relative to the curvature of the object is often non-negligible. As AFM is progressing toward measuring increasingly smaller objects (e.g., proteins and virus capsids [10–12]), there is a growing need to better understand how the curvature of the probe and the nature of the indenter–object contact affect the mechanical response [13].

The mechanics of shells is strongly linked to their geometry [14,15] and, for a shell with positive Gaussian curvature, bending and stretching are inherently coupled. The deformation of a shell is primarily governed by a need to minimize the energetically costly stretching, in favor of bending, thereby preserving the isometry of the surface. In the linear regime, there has been a substantial body of work centered on rationalizing this interplay, from the seminal work of Reissner [16] on spherical shells to the more recent study of geometry-induced rigidity in nonspherical pressurized shells [17,18]. Past the linear regime, Pogorelov [19] developed a theory for the formation of an axisymmetric ridge on an indented shell. This description is, however, not valid for deformations large enough to cause nonaxisymmetric buckling and the development of sharp angular features [20–22], for which a general predictive framework does not yet exist.

The study of the large deformations of shells under indentation typically involves either point or plate loading. Vaziri and Mahadevan [20] conducted a numerical investigation of an elastic hemispherical shell under point indentation using finite element modeling (FEM). They found that, past the linear regime, the circular ridge loses axisymmetry, whereby three sharp vertices of localized deformation form. Vaziri [21] has also studied the case of plate indentation. Experimentally, localization in ping pong balls has been studied by either indenting a single ball or compressing packings of balls [23,24]. The effect of plasticity in the localization during the indentation of metallic shells has also been investigated, in both numerical simulations and experiments [25–27]. We have also performed a detailed experimental investigation of the formation of localized structures in thin elastomeric shells under indentation [22], which we review in more detail in Sec. 2.

Some similarities can be established between the localized structures found in doubly-curved shells and those of developable surfaces (e.g., plates, as well as conical, and cylindrical shells). For example, when a plate is placed under boundary-imposed geometric constraints, crumpling can occur such that energy is localized along *ridges* and vertices, known as *d-cones*, for "developable cones" [15,28]. This focusing of the energy along small regions minimizes stretching energy globally and allows the rest of the surface to remain developable. These two classes of localized structures, ridges and d-cones, have been well studied and characterized through experimental, numerical, and theoretical work [15,28]. Drawing an analogy with d-cones in plates and cylindrical shells [29], we designate the localized objects in doubly-curved shells as *s-cones*, short for "shell cones," emphasizing that doubly-curved shells are not developable.

Here, we conduct a series of numerical experiments on the indentation of thin elastic shells and take advantage of the predictive power of FEM for this class of problems that we previously validated against our own precision experiments [22]. We perform a systematic parametric study to gain detailed physical insight into the localization process, in a way that would be challenging

Contributed by the Applied Mechanics Division of ASME for publication in the Journal of Applied Mechanics. Manuscript received September 16, 2014; final manuscript received October 9, 2014; accepted manuscript posted October 15, 2014; published online October 30, 2014. Editor: Yonggang Huang.

to accomplish through physical experiments. In Sec. 2, we start by defining the problem and reviewing our own previous experiments. The numerics are introduced in Sec. 3. In Sec. 4, we explore whether the self-weight of the shell has an effect on the mechanical response. We then study how the localization process depends on the radius of the shell and on the ratio between the thickness and shell radius, in Sec. 5. A comparison between using a linearly elastic versus a neo-Hookean (NH) material model is studied in Sec. 6 and the maximum principal strains during localization are quantified in Sec. 7. Finally, in Sec. 8, we investigate the role of friction of the shell–indenter contact in localization.

2 Problem Definition and Review of Our Previous Work

We start by reviewing our previous experimental and numeric study [22] on the localization of deformation during the indentation of a thin elastic shell, which also serves to define the problem. In Fig. 1, we show the case of point indentation (indenters with other radii are discussed below). In the experiments, the thin shells were fabricated out of Vinlypolysiloxane (VPS), a silicone-based rubber, with Young's modulus $E = 1.36\,\text{MPa}$, radius $R_1 = 25\,\text{mm}$, and thickness $t = 0.3 \pm 0.01\,\text{mm}$. The hemispherical shell was clamped horizontally at its equator and an indentation load was then applied to the pole of the shell, along its vertical axis (see Fig. 1(*a*)). The evolution of the deformation upon indentation was captured by digital imaging, as shown at the representative stages of indentation in Figs. 1(*a*) and 1(*b*). The dimensionless indentation was defined as $\varepsilon = \delta/R_1$, where δ is the indentation displacement, which was increased quasi-statically at the rate of $\dot{\delta} = 5\text{mm}/\text{min}$. The white lines in the photographs of Fig. 1(*b*) correspond to light reflections from the ridgelike regions, where the shell inverts. The FEM simulations (Fig. 1(*c*)) provided the energy density, as indicated by the color map in the figure, and localized structures were associated with sharp local increases in energy density. Excellent qualitative and quantitative agreement was found, throughout, between experiments and FEM simulations [22].

During point indentation (Fig. 1), in the range $0.02 < \varepsilon < 0.29$, the cap of the shell first inverts inward, forming an axisymmetric (Pogorelov) ridge [19], along which the shell stretches

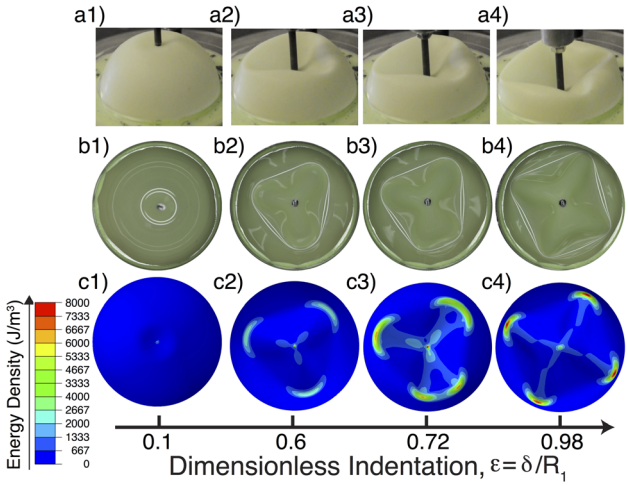

Fig. 1 Point indentation. (*a*) Experimental snapshots (axonometric view) of the evolution of the pattern of localization for an elastomeric shell under point indentation at its pole. (*b*) Experimental snapshots captured from underneath the shell. The white reflection corresponds to the location at which the shell inverts. (*c*) Snapshots from FEM simulations of the same scenario corresponding to (*b*). Color map represents the strain energy density. Further details on the material and geometric properties are given in the text.

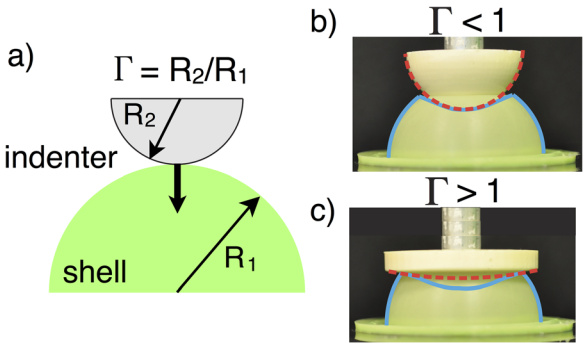

Fig. 2 Changing the shape of the indenter. (*a*) Schematic of the indentation of a shell by an indenter of radii R_1 and R_2, respectively. The indenter to shell ratio is $\Gamma = R_2/R_1$. (*b*) Sharp indenters ($\Gamma < 1$) remain in contact with the pole of the shell during indentation. (*c*) Blunt indenters ($\Gamma > 1$) delaminate from the pole of the shell during indentation.

(Figs. 1(*a*1) and 1(*b*1)). Past a critical value of indentation ($\varepsilon_c \sim 0.30$), the ridge loses axisymmetry; strain focuses (Figs. 1(*a*2) and 1(*b*2)) at three conical-like vertices, the *s-cones*, and the inverted portion of the shell develops a tetrahedral shape. These three s-cones are connected by straight segments, which we designate as *ridges*, acting as folds between the mostly undeformed outer shell and the inner inverted region. Inside the inverted tetrahedral region, additional folds form, which we refer to as *gullies* that connect each of the s-cones to the point of indentation. As the shell is indented further, the s-cones travel along the surface of the shell and eventually new s-cones form by the splitting of an existing one (Figs. 1(*a*3) and 1(*b*3)) resulting in four well defined s-cones (Figs. 1(*a*4) and 1(*b*4)).

In Ref. [22], we also considered the effect of changing the radius of curvature of the indenter, R_2. The indenter to shell ratio, $\Gamma = R_2/R_1$ (see Fig. 2(*a*) for schematic), was varied from $\Gamma = 0$ (point load) to $\Gamma = \infty$ (plate load), with 12 values in-between. The nature of the indenter–shell contact is qualitatively different for blunt indenters ($\Gamma > 1$) and sharp indenters ($\Gamma < 1$). For sharp indenters, the pole of the shell and indenter remains in contact throughout indentation (Fig. 2(*b*)), whereas for blunt indenters, the shell delaminates from the pole of the indenter (Fig. 2(*c*)). Therefore, the shape of the indenter has a marked effect on various aspects of the localization process including: its onset, the number of s-cones that form and the overall mechanical response. Moreover, we also found that Γ had an important influence on the frictional contact with the shell such that friction had to be included in the FEM simulations in order to produce good quantitative agreement with experiments.

3 FEM of an Indented Shell

Guided by the excellent quantitative agreement between experiments and FEM simulations obtained in our previous study [22], which validates the numerics, the remainder of this paper focuses on significantly extending our numerical exploration to perform a systematic study of parameter space. Our FEM simulations are performed using the commercial finite element package ABAQUS/CAE. The hemispherical shell is modeled with a clamped boundary condition at its equator and each indenter is modeled as a rigid sphere with a displacement-control boundary condition. The indenters-to-shell radii ratio, $\Gamma = R_2/R_1$ is varied by changing R_2, while keeping R_1 constant. For the material properties of the shell, we use a NH hyperelastic model (with the exception of Sec. 6, where we compare the results to the LE case). The NH strain energy potential is

$$W = \frac{\mu}{2}(\bar{I}_1 - 3) + \frac{K}{2}(J-1)^2 \tag{1}$$

where J is the total volume ratio, and $\bar{I}_1 = \bar{\lambda}_1^2 + \bar{\lambda}_2^2 + \bar{\lambda}_3^2$, where $\bar{\lambda}_i = J^{-1/3}\lambda_i$ and λ_i are the principal stretches. Unless stated otherwise, we take the shear and bulk moduli to be $\mu = 454.5$ kPa and $K = 85.11$ MPa, respectively, which describe the VPS material previously used in the experiments [22]. The density of VPS is $\rho = 1200\,\text{kg/m}^3$.

Four-node thin shell elements with reduced integration (element type S4R) were used in all simulations with a free mesh scheme and no initial geometric or material imperfection is included in the computational model. These S4R elements are general purpose shell elements that implement Kirchoff shell theory in the thin shell limit. A mesh sensitivity study verified that the results were independent of the element size. To capture the local instabilities, we used a stabilizing mechanism (available in ABAQUS/Standard solver) based on the automatic addition of volume-proportional damping, which is decreased systematically to ensure that the response was insensitive to this change. The chosen conditions (free mesh, geometric nonlinearity, and displacement controlled indentation under quasi-static conditions) were sufficient to obtain a controlled postbuckling response, without a need to feed the structure with imperfections nor perform a RIKS analysis. Friction is modeled as a penalty formulation with a standard Coulomb friction coefficient.

4 Self-Weight of the Shell

We first investigate how the self-weight of the shell affects the mechanical response during indentation, focusing on the case of point loading described in Sec. 2, for a shell with $t/R_1 = 0.01$. In Fig. 3(*a*), we plot the indentation load, P, as a function of dimensionless indentation, ε, and compare the two cases of excluding (P_{without}, solid line) and including (P_{with}, dashed line) self-weight of the shell. The two vertical dashed lines at $\varepsilon = 0.21$ and $\varepsilon = 0.67$ indicate the critical indentations at which three and four s-cones form, respectively. For small values of ε, both cases (inclusion versus exclusion of self-weight) exhibit nearly identical load-indentation curves, demonstrating that the weight of the shell has little effect prior to the formation of s-cones. The two curves then start to deviate from each after $\varepsilon \gtrsim 0.21$ and we further quantify this relative deviation by the ratio

$$\varphi(\varepsilon) = \frac{P_{\text{without}} - P_{\text{with}}}{(P_{\text{without}} + P_{\text{with}})/2} \tag{2}$$

In Fig. 3(*b*), we plot $\varphi(\varepsilon)$ and find that it remains small ($\lesssim 10\%$), especially for the values of indentation of interest, $0.21 < \varepsilon < 0.67$, where s-cones first form and evolve. Given that self-weight only has a small effect on the mechanical response in this region of interest, for simplicity we choose to neglect it from here on.

5 Radius and Thickness of the Shell

We now study the effect of the radius of the shell on the formation of s-cones and associated mechanical response, toward probing the universality of the localization process across length scales. In Fig. 4, we present a series of nondimensionalized load-indentation curves for shell indentation under point loading, with radii in the range $0.01 < R_1\ (\text{m}) < 1000$. The loads have been normalized by Et^2, where E is the Young's modulus and t is the thickness of the shell, which is set such that the ratio between the thickness and the radius of the shell remains constant, $t/R_1 = 0.01$. Under this nondimensionalization, the load-indentation curves collapse onto a single master curve, which is significant of scale invariance.

In Fig. 4, we also superpose (vertical solid lines) the mean of critical indentations (for the six values of R_1) at the onset of three and four s-cones, at $\varepsilon = 0.180 \pm 0.005$ and $\varepsilon = 0.710 \pm 0.010$, respectively. The vertical dashed lines in this figure are the corresponding standard deviation for the critical indentations (for the six values of R_1). The mean values of critical indentation at the

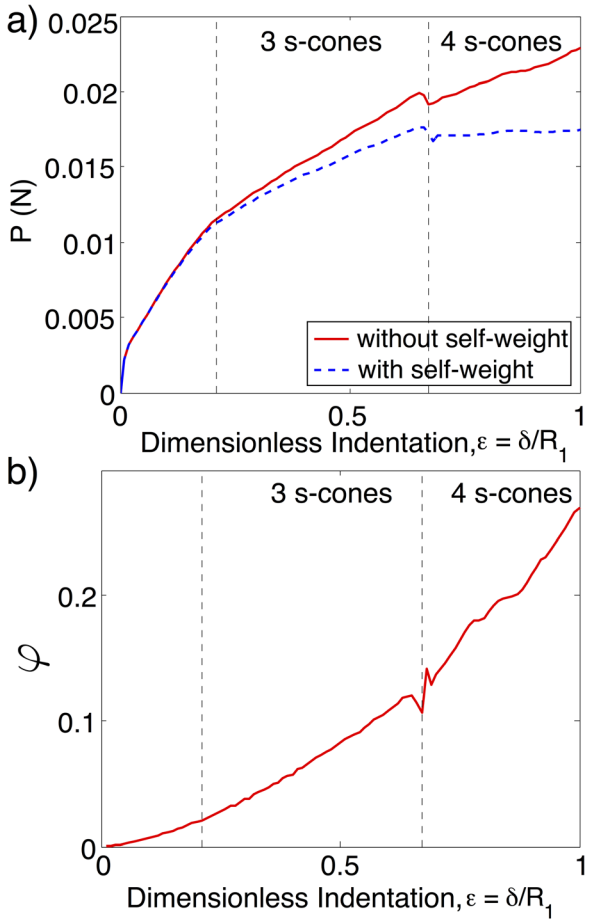

Fig. 3 The effect of self-weight on the mechanical response. The shell thickness to radius ratio is $t/R_1 = 0.012$. (*a*) Load–indentation curves for a shell under point indentation when weight is included (dashed blue) or excluded (solid red). (*b*) Relative difference of the two load curves, φ (defined in Eq. (2)). The vertical dashed lines correspond to indentation values at which three s-cones and four s-cones form, $\varepsilon = 0.21$ and $\varepsilon = 0.69$, respectively.

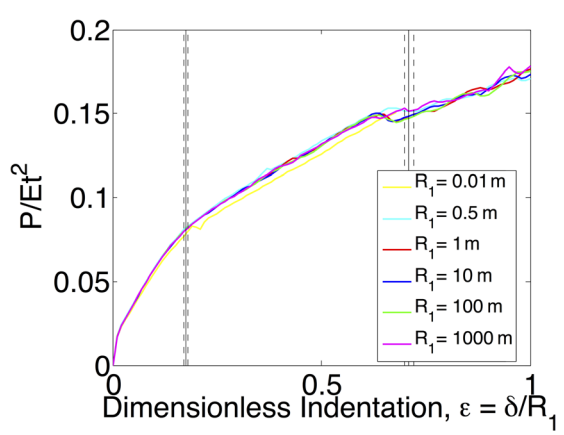

Fig. 4 The effect of shell radius on mechanical response. Nondimensionalized force–indentation curves for shells with various radii, ranging from $R_1 = 0.01$ m to $R_1 = 1000$ m with the same thickness ratio of $t/R_1 = 0.01$. Force is nondimensionalized with the Young's modulus E and thickness t. The solid (dashed) vertical lines correspond to the average (standard deviation) of the critical indentation for the formation of 3 and 4 s-cones (across the six shell radii).

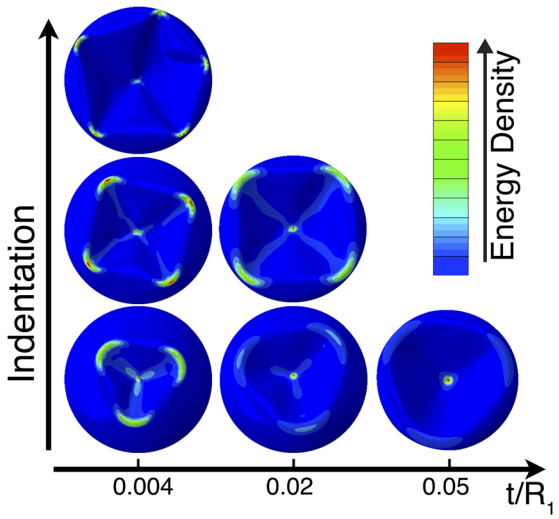

Fig. 5 The effect of shell thickness on the formation and evolution of s-cones. Representative snapshots of shells for $t/R_1 = (0.004, 0.02, 0.05)$, under point indentation. The color map corresponds to strain energy density.

onset of three and four s-cones are nearly identical across the varying shell radii, with small standard deviations from the average values, which further demonstrates the scalability of the localization process across length scales and its strong rooting in geometry.

We now consider the effect of the dimensionless thickness, t/R_1, on the formation of localized structures and conduct simulations (still for point indentation) in the range of $0.001 < t/R_1 < 0.07$. The ratio t/R_1 is varied by keeping $R_1 = 1$ m constant and varying t, with all other parameters constant. In Fig. 5, we present a series of representative surface maps of the strain energy density, W, for shells with different values of t/R_1, for which the formation and evolution of s-cones is qualitatively different. For the thinnest shells ($0.001 \le t/R_1 \le 0.004$), there is first an evolution from three-to-four, then four-to-five s-cones, with the appearance of a new s-cone occurring by splitting of an existing one, similarly to the scenario presented for point indentation in Sec. 2. Shells with an intermediate thickness ($0.005 \le t/R_1 \le 0.02$) exhibit a similar three-to-four evolution but no new s-cones emerge for further indentation. For the thicker shells ($0.03 \le t/R_1 \le 0.06$), three s-cones form at the onset but there is no further evolution upon an increase of indentation. For the thickest shell studied ($t/R_1 = 0.07$), the deformation remains axisymmetric throughout indentation, suggesting that there is a critical thickness ratio, $0.06 < (t/R_1)_c < 0.07$, above which localization is suppressed.

The effect of shell thickness on localization is further quantified by analyzing the strain energy, W, along paths traced over ridges between adjacent s-cones (see the schematic dashed lines in Fig. 6(*a*)). In Fig. 6(*b*), we plot W along these paths for shells in the range $0.002 < t/R_1 < 0.03$, indented up to $\varepsilon = 0.75$ under point load. As the t/R_1 ratio decreases, energy localization increases at the s-cones, relative to the ridges. For thinner shells, energy is focused more sharply at the s-cones, when compared to thicker shells. This sharpness in energy focusing is quantified in Fig. 6(*c*) by plotting the minimum and maximum energy densities, W_{min} and W_{max}, along the traced paths, as a function of t/R_1. The energy density at the s-cones, W_{max}, is approximately independent of t/R_1; $W_{max} = (4.2 \pm 1.3) \times 10^3$ J/m^3. In contrast, the energy at the midpoint of a ridge, W_{min}, increases with t/R_1 in a way that is consistent with the scaling $W_{ridge} \sim t^2$ (the exponent obtained by fitting the data to a power-law is 2.1 ± 0.1), but we have not yet been able to rationalize this finding. It is interesting to note, however, that this scaling is quantitatively different from that of the

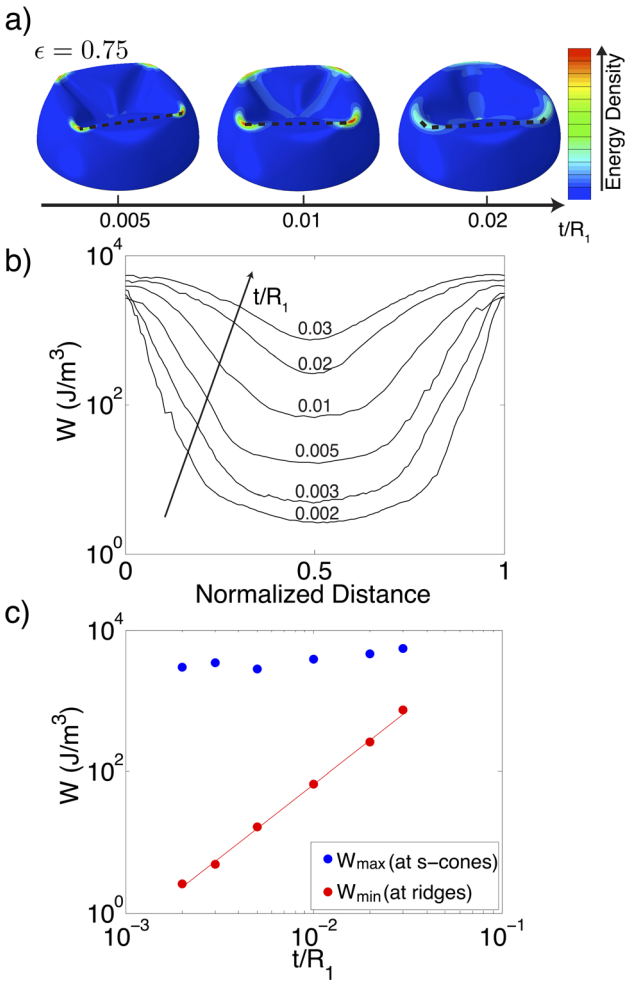

Fig. 6 The effect of shell thickness. (*a*) Snapshots of shells with increasing t/R_1 ratios at $\varepsilon = 0.75$, under point indentation. The color map indicates strain energy density. The black dashed lines trace a path along ridges between adjacent s-cones. (*b*) Strain energy density, W, along the paths in (*a*), for shells with thickness to radius ration in the range $0.002 < t/R_1 < 0.03$, indented to $\varepsilon = 0.75$ under point indentation. (*c*) W_{max} (at the s-cones) and W_{min} (at the ridges), as a function of t/R_1. The solid red line indicates a power-law fit to the data, with exponent 2.1 ± 0.1.

energy along a ridge on a plate, $W_{ridge} \sim t^{8/3}$ [15,30]. As t/R_1 increases, the strain energy becomes less localized at the s-cones in comparison to the ridges.

6 Linear Elastic Versus Neo-Hookean Material Models

The simulations performed thus far used a NH material model, which closely matches the elastomeric VPS shells of the experiments in Ref. [22]. This is in contrast with previous studies of localization in thin shells which used a LE material model [20,21]. Toward better understanding the role of material nonlinearities in the localization process, we directly compare the LE and NH cases for the material reported in Ref. [22] and summarized in Sec. 2. However, note that in both cases, geometric nonlinearities are taken into account in the FEM simulations.

In Fig. 7, we present FEM snapshots of the indented configurations, for the LE (Fig. 7(*a*)) and NH (Fig. 7(*b*)) cases, for a shell with $t/R_1 = 0.012$. These series of snapshots is obtained over a range of shell-to-indenter radii, from point load ($\Gamma = 0$) to plate load ($\Gamma = \infty$). The corresponding configurations in Figs. 7(*a*) and 7(*b*) are obtained for the same value of dimensionless

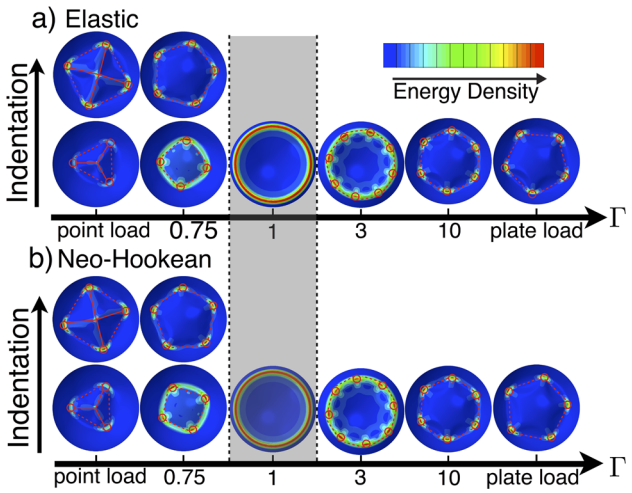

Fig. 7 Deformed configurations of a shell under indentation using (*a*) a LE or (*b*) a NH material model. The shell thickness to radius ratio is $t/R_1 = 0.012$. In both cases the ratio between the radii of the shell and the indenter, is varied from point load ($\Gamma = 0$) to plate load ($\Gamma = \infty$). The color map represents to strain energy density. Red circles indicate the location of s-cones. Dashed lines are drawn over ridges that connect s-cones, along which the curvature of the shell is inverted. Solid red lines are drawn over gullies that connect s-cones to the pole of the shell (only present for point load). No localization occurs with indenters with $\Gamma \sim 1$ (shaded region).

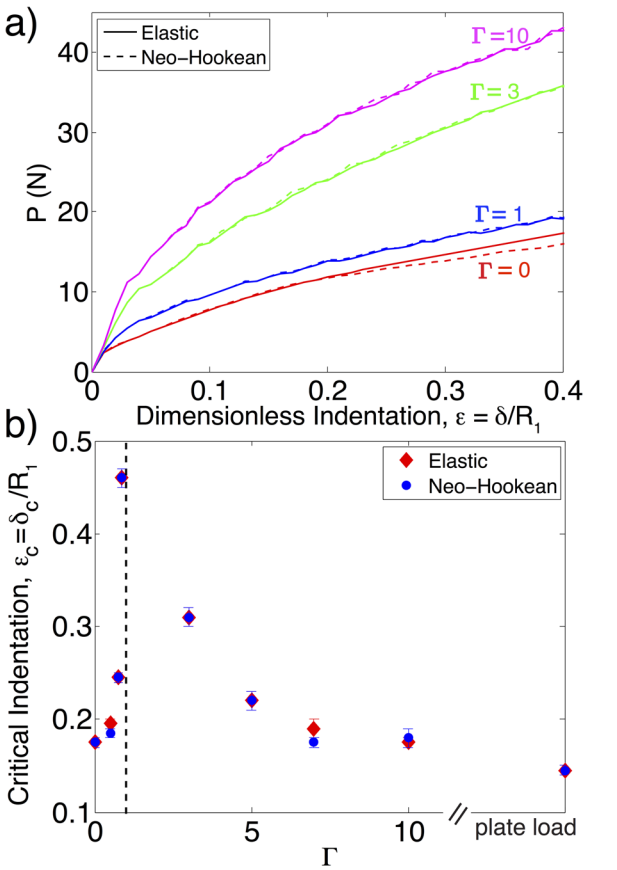

Fig. 8 Quantitative comparison of mechanical response between LE and NH material models. (*a*) Load-indentation curves for a variety of indenters, $\Gamma = (0, 1, 3, 10)$, using the LE (solid lines) and NH (dashed lines) material model. (*b*) Critical indentation at the onset of localization, comparing the LE and NH models. No localization occurs for $\Gamma \sim 1$ (vertical dashed line). The shell thickness to radius is $t/R_1 = 0.012$.

indentation, ε. Localization occurs with all indenters, except for $\Gamma = 1$, where the radius of the indenter is identical to that of the shell and the two surfaces remain in complete contact, thereby preventing the formation of s-cones (identified by the sharp increases in energy density, as above). At the same value of Γ, the number and distribution of s-cones in the LE and NH cases are qualitatively similar. For sharp indenters ($\Gamma < 1$), the number of s-cones increases with indentation and new s-cones emerge by the splitting of an existing one. For blunt indenters ($\Gamma > 1$), the number of s-cones does not evolve after onset, contrary to Ref. [22] where an evolution was also found in this regime. This discrepancy is presumably due to the frictionless assumption in the shell–indenter contact of the simulations shown in Fig. 7 (whereas friction was taken into account in Ref. [22]). The effect of friction will be systematically considered in Sec. 8, below.

To further compare the LE versus NH models, quantitatively, we turn to the mechanical response, as measured by the indentation load, P, as a function of dimensionless indentation, ε. In Fig. 8(*a*), we plot load-indentation curves for different indenters, $\Gamma = (0, 1, 3, 10)$, all of which exhibit a monotonically increasing load and the curves are concave-down. Again, the results obtained with the LE (solid lines) and NH (dashed lines) material model are nearly identical. Moreover, Fig. 8(*b*) presents the critical indentation at which s-cones first form, as a function of Γ for both cases (circles and diamond symbols for the LE and NH model, respectively). The critical indentation has a divergencelike behavior, with the maximum values of the critical indentation found on either side of $\Gamma \sim 1$. Again, we find nearly identical quantitative results between the two material models, and the deviation between the two are within 2%.

7 Maximum Principal Strains During Indentation

Having found that the FEM simulations produce nearly identical results when either a LE or a NH material model is used, we further investigate this finding by quantifying the maximum principal strain, defined locally at the material level, in the shell during indentation. This information would have been possible but challenging to obtain experimentally through 3D digital image correlation (DIC); instead, we take advantage of our numerics given that they have already been carefully validated against experiments [22].

In this section, the VPS material of the shell is modeled as NH, with $R_1 = 1$ m and $t = 0.01$ m. For clarity, we plot the maximum principal strain, ε_{max}, as a function of dimensionless indentation, separately for sharp indenters ($\Gamma \leq 1$, in Fig. 9(*a*)) and for blunt indenters ($\Gamma > 1$, in Fig. 9(*b*)). In all cases, ε_{max} remains small and does not exceed ~6%. We find that ε_{max} first increases sharply in the linear regime, then plateaus as the cap near the pole inverts and the axisymmetric ridge forms. Past the onset of s-cones (marked by a black diamond in each curve of Fig. 9), ε_{max} then increases again, moderately for sharp indenters (Fig. 9(*a*)) and more sharply for bunt indenters (Fig. 9(*b*)). For sharp indenters, the overall value of ε_{max} is largest for point load and decreases with increasing Γ, toward 1. The opposite trend is found for blunt indenters; ε_{max} is largest for plate load and decreases as Γ decreases toward 1.

It is remarkable that, even though the shells undergo significantly large macroscopic deformation during indentation, the local strains remain in the order of a few percent, albeit still localized. This finding supports that the usage of Kirchoff shell theory for this problem (as implemented in the FEM simulations) is appropriate. We recall that Kirchoff's theory is only valid for shear shells and small local strains, i.e., for scenarios in which transverse shear deformations are negligible [14].

In Sec. 6 above, we found that using either a LE or a NH model produced nearly identical results. This can now be attributed to the relatively low values of strains involved, such that the material

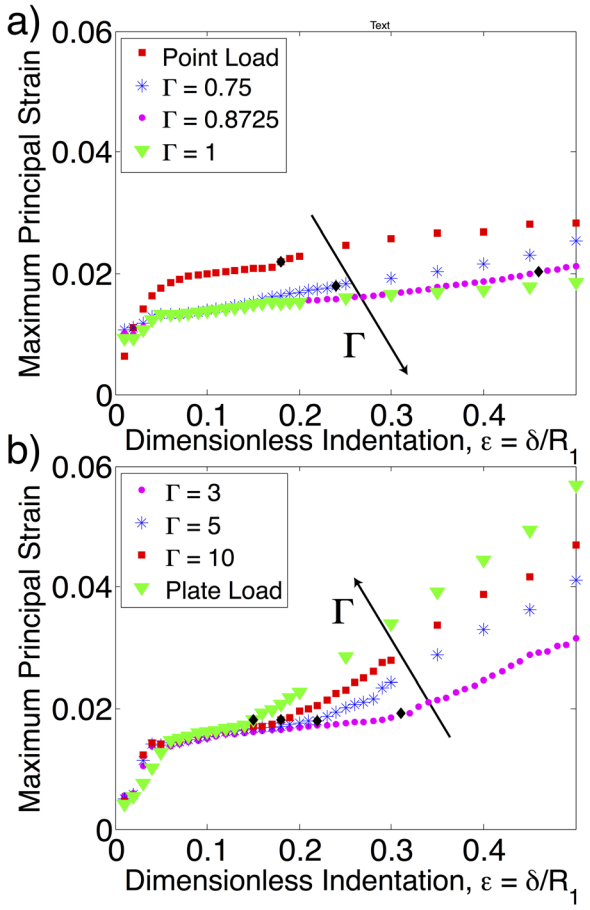

Fig. 9 Maximum principal strain, ε_{max}, during indentation a shell ($t/R_1 = 0.01$) for (*a*) sharp indenters, $\Gamma \leq 1$, and (*b*) blunt indenters, $\Gamma > 1$. The black diamond symbol on each curve indicates the critical indentation at which s-cones form.

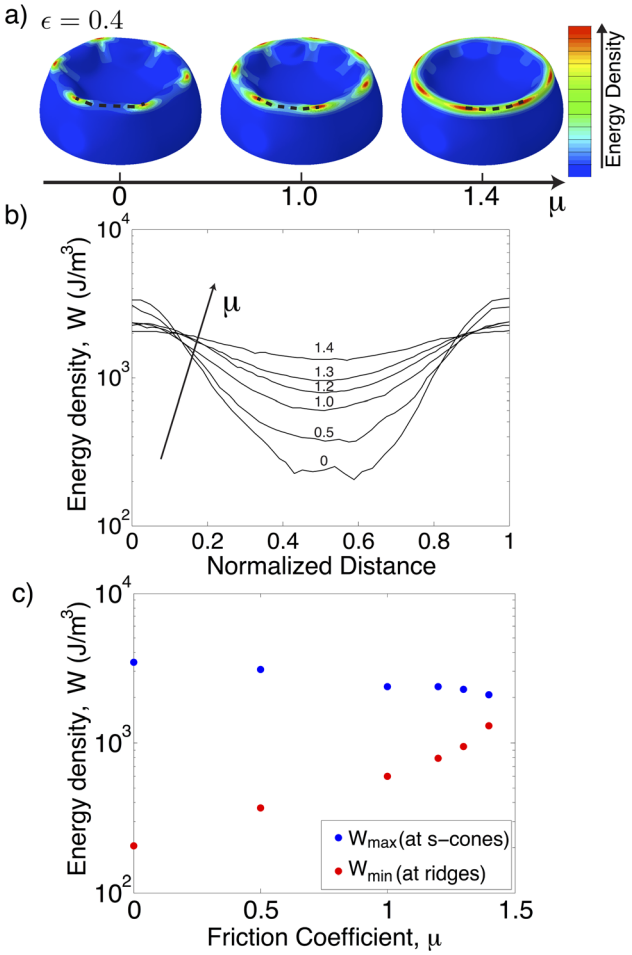

Fig. 10 The effect of friction on localization. (*a*) FEM snapshots for indentation of a shell ($t/R_1 = 0.01$) with $\Gamma = 10$, for various friction coefficients, μ, at $\varepsilon = 0.4$ indentation. The color map indicates strain energy density. (*b*) Strain energy density plotted along paths over ridges between adjacent s-cones, black dashed lines in (*a*), for shells different values of μ. (*c*) W_{max} (at the s-cones) and W_{min} (at the ridges midpoint) as a function of μ.

nonlinearities associated with finite deformations of the hyperelastic material are negligible. Moreover, this finding is also consistent with the excellent quantitative agreement between FEM and experiments obtained in Ref. [22], given that uniaxial mechanical testing of VPS indicates that the response remains linear for strains up to $\approx 10\%$. More generally, these results suggest that whereas plasticity would need to be considered for thin metallic shells under indentation (strains above 1%), many polymeric shells may remain in the linear material regime, even after the onset of s-cones.

8 The Role of Friction

The simulations performed in the sections above assumed a frictionless contact between the shell and the indenter. However, our previous experiments have revealed the important role that friction plays in the mechanical response during indentation [22]. Given that the effect of friction is particularly significant for blunt indenters, we chose to focus on $\Gamma = 10$, as representative of this regime. We proceed by systematically exploring the shell–indenter frictional contact in this problem, using FEM, with a variety of friction coefficients ranging from $\mu = 0$ to 1.7 (for a shell with $t/R_1 = 0.01$).

In Fig. 10(*a*), we show representative snapshots of the indented shell, at $\varepsilon = 0.4$, for increasing values of friction coefficient, where the number of s-cones is found to increase with μ. Six, seven, and eight s-cones form for $\mu = 0$, 1, and 1.4, respectively, and for $\mu > 1.5$, the deformation remains axisymmetric and no s-cones appear. For $\mu = 1.7$, the largest value explored, the shell eventually undergoes global buckling, whereby the sides of the shell cave inward, near the base of the shell, developing a pattern of five horizontal dimples (see Fig. 11). The study of this global buckling regime is outside the scope of this paper.

We return to the strain energy density, W, to gain more insight into how friction affects the distribution of localized strain energy. In Fig. 10(*b*), we plot W along a path traced over the ridges between two neighboring s-cones (dashed line in Fig. 10(*a*)), for different values of μ. The energy becomes less sharply focused at s-cones relative to the ridges, as μ increases. The maximum and minimum of the energy density, W_{max} (at the s-cones) and W_{min} (at the ridge midpoint), respectively, are plotted in Fig. 10(*c*) as a function of μ. As the friction coefficient μ increases, the energy is reduced at the s-cones and increased at the ridge midpoint, and both eventually converge to the same value ($\sim 2 \times 10^3 \text{J/m}^3$) when $\mu \sim 1.5$. Coincidentally, this is the value of the friction coefficient, beyond which no localization is observed and the deformation is essentially axisymmetric, as mentioned above.

Next, we quantify the critical indentation for the onset of localization as a function of μ (Fig. 12(*a*)). The formation of s-cones is delayed for increasing values of the friction coefficient μ, and the critical indentation asymptotes to $\varepsilon_c = 0.18$, as μ decreases toward 0. The dependence of the reaction force at the critical indentation versus μ is plotted in Fig. 12(*b*). Similarly to the $\varepsilon_c(\mu)$ dependence, the reaction load at the critical indentation increases with μ and

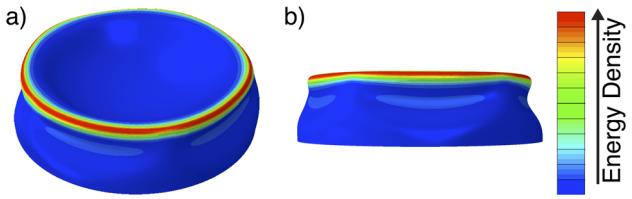

Fig. 11 (*a*) Isometric view of the global buckling mode for a shell ($t/R_1 = 0.01$) under large indentations (configuration shown at $\varepsilon = 0.51$) for an indenter with $\Gamma = 10$ and $\mu = 1.7$. (*b*) Side view. Color map indicates strain energy density.

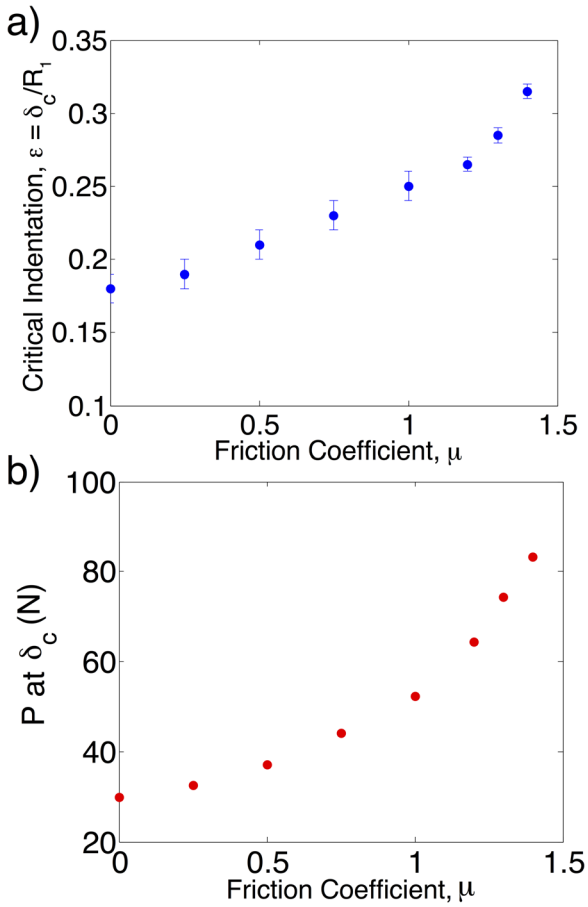

Fig. 12 (*a*) The critical indentation for the onset of localization for an indenter with $\Gamma = 10$ versus μ. (*b*) Load, *P*, at the critical indentation, versus μ. The shell thickness to radius ratio is $t/R_1 = 0.01$.

asymptotes to $P(\delta_c) \simeq 30\,\mathrm{N}$, as μ decreases toward 0. These two results suggest that rougher shells (higher friction coefficients) are more resistant to localization and have a higher load-bearing capacity.

In Fig. 13, we plot load-indentation curves for different values of the friction coefficient and find that *P* significantly increases with μ, especially in the regime where localization occurs ($\varepsilon \gtrsim 0.2$). For low values of the friction coefficients, $\mu < 1$, the load-indentation curves have a concave-down shape in which the load asymptotically tends to an approximately constant value. In contrast, for large friction coefficients $\mu > 1$, the load-indentation curves have inflection points, after which the curves have a concave-up shape. These results suggest that the shell–indenter frictional contact can be tuned to dramatically modify the mechanical response of the shell under indentation.

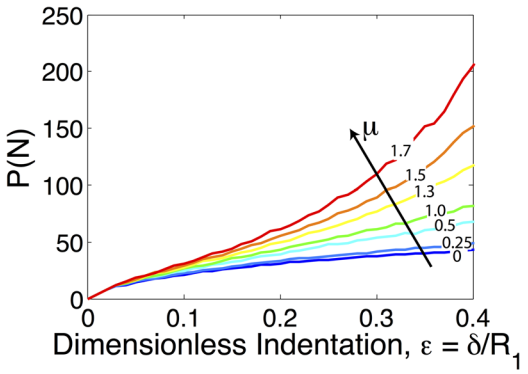

Fig. 13 The effect of friction on the mechanical response. Load-indentation curves for an indenter with $\Gamma = 10$ for friction coefficients $\mu = 0, 0.25, 0.5, 1.0, 1.3, 1.5, 1.7$.

9 Discussion and Conclusions

We have presented systematic results of an FEM numerical exploration on the large deformation of indented thin elastic spherical shells. Our FEM simulations had previously been accurately validated against experiments. The curvature of the indenter was found to strongly effect the onset and evolution of localized structures, which we labeled as s-cones. Moreover, by varying the radius of the shell, while keeping the thickness-to-radius ratio t/R_1 constant, we presented evidence for the scale-invariance of the localization in indented shells. This finding suggests that our results should be relevant and applicable for engineering scenarios across a wide range of length scales. The thickness of the shell when compared to its radius does, however, affect the pattern of s-cones at onset, their evolution of s-cones, and whether or not they form at all. The extent of localization as measured by the strain energy density stored also depends strongly on the thickness of the shell; it is more pronouncedly localized at the s-cones for thin shells than in thick shells.

Even though shells under indentation can undergo large macroscopic deformation, the local material strains remain relatively small, less than 6%, throughout the process. As a result, the nonlinearities of the hyperelastic material considered are negligible, such that using either a LE or NH yields nearly identical results. This indicates that our results are applicable beyond elastomeric shells and can be extended to other materials that remain in the elastic regime up to a few percent strain, provided that no plasticity takes place. Moreover, the fact that large macroscopic deformations of our shells are achieved with relatively small values of local strains, proposes that localized structures such as s-cones, ridges, and gullies may be employed as energetically efficient hinges, for the design of foldable (e.g., origami) shell structures.

The frictional shell–indenter contact dramatically affects the mechanical response of the shells and modifies their load-bearing capacity, especially for blunt indenters. Moreover, higher values of the friction coefficient between the shell and the indenter can lead to the suppression of localization. This finding, in conjunction with the observation of increased load-bearing capability for rough shell–indenter contact, could have implications for the design of engineering shells with enhanced resistance to localization by roughening their surfaces.

The robustness of the localization behavior that we have uncovered for shells under indentation emphasizes the prominent interplay between geometry and mechanics in this class of problems. We hope that our exploratory numerically study will help catalyze further theoretical efforts in this direction. Moreover, our work has focused on elastic systems and it would be interesting to perform a similar analysis for metallic shells that undergo elastic–plastic deformation.

Acknowledgment

We are grateful to Ashkan Vaziri and Amin Adjari for fruitful discussions. A.N. acknowledges the support of NSF through a Graduate Research Fellowship (1122374) and MIT through an Asher H. Shapiro Graduate Fellowship. P.M.R. thanks support from the National Science Foundation, CMMI-1351449 (CAREER).

References

[1] Wempner, G., and Talaslidis, D., 2002, *Mechanics of Solids and Shells: Theories and Approximations*, Vol. 24, CRC Press, Boca Raton, FL.
[2] Zhang, X., 1998, "Impact Damage in Composite Aircraft Structures—Experimental Testing and Numerical Simulation," Proc. Inst. Mech. Eng. Part G: J. Aerosp. Eng., **212**(4), pp. 245–259.
[3] Johnson, W., and Mamalis, A., 1978, *Crashworthiness of Vehicles*, Mechanical Engineering Publications, Bury St. Edmunds, UK. Available at: http://trid.trb.org/view.aspx?id=80587
[4] Datta, S. S., Kim, S.-H., Paulose, J., Abbaspourrad, A., Nelson, D. R., and Weitz, D. A., 2012, "Delayed Buckling and Guided Folding of Inhomogeneous Capsules," Phys. Rev. Lett., **109**(13), p. 134302.
[5] Quilliet, C., Zoldesi, C., Riera, C., Van Blaaderen, A., and Imhof, A., 2008, "Anisotropic Colloids Through Non-Trivial Buckling," Eur. Phys. J. E, **27**(1), pp. 13–20.
[6] Arnoldi, M., Fritz, M., Bäuerlein, E., Radmacher, M., Sackmann, E., and Boulbitch, A., 2000, "Bacterial Turgor Pressure can be Measured by Atomic Force Microscopy," Phys. Rev. E, **62**(1 Pt B), pp. 1034–1044.
[7] Roos, W., Bruinsma, R., and Wuite, G., 2010, "Physical Virology," Nat. Phys., **6**(10), pp. 733–743.
[8] Baclayon, M., Wuite, G., and Roos, W., 2010, "Imaging and Manipulation of Single Viruses by Atomic Force Microscopy," Soft Matter, **6**(21), pp. 5273–5285.
[9] Dubreuil, F., Elsner, N., and Fery, A., 2003, "Elastic Properties of Polyelectrolyte Capsules Studied by Atomic-Force Microscopy and RICM," Eur. Phys. J. E, **12**(2), pp. 215–221.
[10] Foucher, J., Schmidt, S. W., Penzkofer, C., and Irmer, B., 2012, "Overcoming Silicon Limitations: New 3D-AFM Carbon Tips With Constantly High-Resolution for Sub-28nm Node Semiconductor Requirements," Proc. SPIE, **8234**, p. 832432.
[11] Roos, W. H., Gibbons, M. M., Arkhipov, A., Uetrecht, C., Watts, N., Wingfield, P., Steven, A. C., Heck, A. J., Schulten, K., Klug, W. S., and Wuite, G., 2010, "Squeezing Protein Shells: How Continuum Elastic Models, Molecular Dynamics Simulations, and Experiments Coalesce at the Nanoscale," Biophys. J., **99**(4), pp. 1175–1181.
[12] Roos, W. H., Radtke, K., Kniesmeijer, E., Geertsema, H., Sodeik, B., and Wuite, G. J., 2009, "Scaffold Expulsion and Genome Packaging Trigger Stabilization of Herpes Simplex Virus Capsids," Proc. Natl. Acad. Sci. U.S.A., **106**(24), pp. 9673–9678.
[13] Costa, K., and Yin, F., 1999, "Analysis of Indentation: Implications for Measuring Mechanical Properties With Atomic Force Microscopy," ASME J. Biomech. Eng., **121**(5), pp. 462–471.
[14] Timoshenko, S., Woinowsky-Krieger, S., and Woinowsky, S., 1959, *Theory of Plates and Shells*, Vol. 2, McGraw-Hill, New York.
[15] Audoly, B., and Pomeau, Y., 2010, *Elasticity and Geometry: From Hair Curls to the Non-Linear Response of Shells*, Oxford University Press, Oxford, NY.
[16] Reissner, E., 1946, "Stresses and Small Displacements of Shallow Spherical Shells," J. Math. Phys., **25**(4), pp. 279–300.
[17] Lazarus, A., Florijn, H. C. B., and Reis, P. M., 2012, "Geometry-Induced Rigidity in Nonspherical Pressurized Elastic Shells," Phys. Rev. Lett., **109**(14), p. 144301.
[18] Vella, D., Ajdari, A., Vaziri, A., and Boudaoud, A., 2012, "Indentation of Ellipsoidal and Cylindrical Elastic Shells," Phys. Rev. Lett., **109**(14), p. 144302.
[19] Pogorelov, A., 1988, *Bendings of Surfaces and Stability of Shells* (Translations of Mathematical Monographs, Vol. 72), American Mathematical Society, Providence, RI.
[20] Vaziri, A., and Mahadevan, L., 2008, "Localized and Extended Deformations of Elastic Shells," Proc. Natl. Acad. Sci. U.S.A., **105**(23), pp. 7913–7918.
[21] Vaziri, A., 2009, "Mechanics of Highly Deformed Elastic Shells," Thin-Walled Struct., **47**(6–7), pp. 692–700.
[22] Nasto, A., Ajdari, A., Lazarus, A., Vaziri, A., and Reis, P. M., 2013, "Localization of Deformation in Thin Shells Under Indentation," Soft Matter, **9**(29), pp. 6796–6803.
[23] Ruan, H., Gao, Z., and Yu, T., 2006, "Crushing of Thin-Walled Spheres and Sphere Arrays," Int. J. Mech. Sci., **48**(2), pp. 117–133.
[24] Dong, X., Gao, Z., and Yu, T., 2008, "Dynamic Crushing of Thin-Walled Spheres: An Experimental Study," Int. J. Impact. Eng., **35**(8), pp. 717–726.
[25] Amiri, S. N., and Rasheed, H. A., 2012, "Plastic Buckling of Thin Hemispherical Shell Subjected to Concentrated Load at the Apex," Thin-Walled Struct., **53**, pp. 72–82.
[26] Gupta, N., Easwara Prasad, G., and Gupta, S., 1999, "Axial Compression of Metallic Spherical Shells Between Rigid Plates," Thin-Walled Struct., **34**(1), pp. 21–41.
[27] Kitching, R., Houlston, R., and Johnson, W., 1975, "A Theoretical and Experimental Study of Hemispherical Shells Subjected to Axial Loads Between Flat Plates," Int. J. Mech. Sci., **17**(11), pp. 693–703.
[28] Witten, T., 2007, "Stress Focusing in Elastic Sheets," Rev. Mod. Phys., **79**(2), p. 643.
[29] Hamm, E., Roman, B., and Melo, F., 2004, "Dynamics of Developable Cones Under Shear," Phys. Rev. E, **70**(2), p. 026607.
[30] Lobkovsky, A. E., 1996, "Boundary Layer Analysis of the Ridge Singularity in a Thin Plate," Phys. Rev. E, **53**(4), pp. 3750–3759.